Journal of Materials Processing Tech. 299 (2022) 117356

Contents lists available at ScienceDirect

Journal of Materials Processing Tech.

journal homepage: www.elsevier.com/locate/jmatprotec

A novel finishing approach for 3D printed inconel 718 by utilizing isotropic electrochemical etching

Khan Muhammad Ajmal, Rong Yi, Zejin Zhan, Jianwei Ji, Linfeng Zhang, Hui Deng *

Department of Mechanical and Energy Engineering, Southern University of Science and Technology, No. 1088, Xueyuan Road, Shenzhen, Guangdong, 518055, China

ARTICLE INFO

Associate Editor: A. Clare

Keywords:
Additive manufacturing
Electrochemical
Inconel 718
Isotropic etching polishing
Mechanical properties
Surface roughness

ABSTRACT

In this study, a novel and highly efficient isotropic etching polishing (IEP) technique electrochemically polished flat and complex 3D printed Inconel 718 (IN718) parts. The anisotropic etching was transformed into isotropic etching based on the electrolyte diffusion characteristics, and the latter was also realized as the polishing mechanism of 3D printed IN718. Wet etching revealed inhomogeneous microstructures in 3D printed IN718, which dissolved preferentially when polished for a longer duration. The initial surface roughness of 674 nm was reduced to 31.5 nm, and a maximum of 2.42 mm^3/min material removal rate (MRR) was achieved that varied with IEP parameters. The IEP improved the corrosion resistance of 3D printed IN718 compared to the original and grounded substrates, but it was limited by the processing time. Contrarily, the surface mechanical properties of 3D printed IN718 were slightly degraded after IEP. Finally, the 3D printed IN718 complex parts were polished for 5 min, and the Sa roughness was reduced by 76 %, demonstrating a huge potential of IEP as a contemporary industrial polishing technique.

1. Introduction

Aerospace and aeronautics are among the most imminent sectors in the modern era appealing for materials with highly reliable mechanical properties and efficient performance under extreme conditions. Ulutan and Ozel (2011) mentioned that the austenitic nickel superalloy Inconel 718 (IN718) has characteristic mechanical properties such as creep behavior, high fatigue and corrosion resistance, and high thermal strength. These typical mechanical properties are prerequisites for manufactured parts such as high-pressure exhaust pipes, nozzles, and turbine discs blades, which are widely used in the hot sections of space vehicles, submarines, and nuclear power plants (Mahalle et al., 2019).

Additive manufacturing (AM) has drawn considerable attention as an advanced end used metal parts fabrication technique since the last decade. AM is an energy-efficient, cost-effective, and relatively quick technique because of the layer-by-layer allocation of base materials and low buy-to-fly ratio based on the material addition approach, as Thijs et al. (2010) mentioned. According to Han (2017), AM can be a potential applicant for manufacturing over 75 % aero-engine parts, and nickel-based alloys can be the most vibrant base materials. However, in addition to the conventional machining challenges of IN718, such as low thermal conductivity (11 W/m °C), machine hardening behavior, and high strength, as mentioned by Mahalle et al. (2019); layer by layer deposition manufacturing of metal parts by selective laser melting (SLM) is susceptible to partial remelting and attachment of unmelted particles resulting in poor surface finish, while strong temperature gradients cause characteristic irregularities in microstructures as discussed by Kaynak and Tascioglu (2019). These abnormalities reinforce when fabricating complex geometries, especially with intricate internal features. According to Greitemeier et al. (2016), the surface roughness strongly influences the fatigue life of parts produced by AM. Therefore, post-processing of the 3D printed IN718 parts for improving surface roughness and residual stress is indispensable.

To date, different post-manufacturing finishing techniques have been used to improve the surface quality of 3D printed parts. These techniques encompass conventional mechanical polishing, chemical polishing, electrochemical polishing, laser polishing, and the combination of different finishing methods. For example, Mohammadian et al. (2018) found that synergistic application of chemical and abrasive flow polishing is befitting to remove semi-weld particles from the outer surface and improve the internal cavities of AM IN625. Li et al. (2020) found that laser polishing reduced the surface porosity of SLM IN718 by 65.7 %. Both the as-received and laser-polished surfaces contained similar phases, but the laser polished surface showed preferential growth of

* Corresponding author.
E-mail address: dengh@sustech.edu.cn (H. Deng).

https://doi.org/10.1016/j.jmatprotec.2021.117356
Received 31 May 2021; Received in revised form 23 August 2021; Accepted 28 August 2021
Available online 1 September 2021

different phases and the formation of heat affected zones (HAZ). Tian et al. (2018) employed laser polishing to improve the surface quality of the AM Ti6Al4V component. Although the surface roughness was reduced to 0.51 μm and the AM defects were removed, extreme changes were induced in the grain structure. According to De Giorgi et al. (2016), a test chamber must artificially maintain an inert environment to prevent metallic oxidation during laser polishing, increasing the complexity and operating cost. Besides, subsurface residual stress on substrates requires repeated laser beam rastering which causes surface hardening. Despite significantly improving the surface roughness of AM parts by the previously mentioned techniques, it is still challenging to polish complex geometries.

Electrochemical polishing (ECP) has been one of the finest approaches for processing extremely rough and high aspect ratio 3D printed metallic surfaces. Zhao et al. (2021) developed an electrochemical mechanical polishing (ECMP) process to remove partially melted powders from the internal holes of AM parts. The mechanical effect during ECP significantly reduced surface fluctuation, discharge gas bubbles, and electrolytic products to achieve a topographically fluctuation-free surface. Urlea and Brailovski (2017) studied the effect of applied potential and cycling time to best optimize the electropolishing of AM IN625 surface with large scatter and achieved up to 82 % improvement in the surface roughness. Similarly, Baicheng et al. (2017) used pre-optimized electrochemical polishing parameters to improve the AM IN718 surface. The achieved surface roughness was still very high (several micrometers), and the polishing mechanism remained unclear. In addition, the effect of the longer polishing duration on surface corrosion characteristics and mechanical properties was not evaluated. Guo et al. (2018a) discovered that high current density results in relatively smooth surface morphologies due to the electrochemical dissolution of different metallic phases and surface products in AM IN718. Besides, the surface energy difference between horizontal and vertical sections of AM IN718 did not influence their dissolution because of the viscous layer effect. Zhang et al. (2020) reported an increase in the electrochemical dissolution anisotropy between horizontal and vertical sections of the as-deposited AM IN718 after the double aging treatment. Anyway, the polishing efficiency of ECP is challenged by the consistent habitation of the viscous layer, which results in relatively higher energy consumption. According to Jacquet (1936), the initial condition of the substrate defines the thickness and electrical resistance of the viscous layer. Recently, Yi et al. (2020) proposed an isotropic etching polishing (IEP) technique based on the merging of isotropic etching holes formed due to the breakdown of the passivation layer. IEP is an energy-efficient electrochemical polishing technique whose polishing mechanism is entirely different from conventional ECP. IEP has been successfully applied to polish different metals and alloys such as Ti, Ni, TC4, and stainless steel 304. According to Fang (2020), future industries seek atomic and close-to-atomic scale manufacturing (ACSM) involving direct processing at the atomic level. Recently, Khan et al., 2021 achieved subnanometer surface roughness of mechanically manufactured IN718 by using IEP, which proves IEP a potential ACSM technique of the futuristic era. After all, uniform polishing of complex geometries and a balance between the surface finish and accuracy is a generic challenge.

The current study is the first of its kind to investigate the IEP of SLM manufactured IN718 flat substrates and complex 3D geometries, such as Southern University of Science and Technology (SUSTech) logos, turbine blade, and nozzle. Chemical etching was used to exposed microstructures in the 3D printed IN718. The electrochemical anisotropic etching of 3D printed IN718 was experimentally transformed into isotropic etching, which was subsequently realized as the polishing mechanism of the 3D printed IN718. In addition, the surface characteristics such as morphology, roughness, contour profiles, and power spectral density (PSD), electrochemical corrosion characteristics, and mechanical properties of 3D printed IN718 were further investigated as a function of the IEP duration.

2. Material and experiments

2.1. Material characterization

The IN718 powder with the diameter varying from 15−53 μm was SLM 3D printed to manufacture discs and complex geometries used in this study. The 3D printing was conducted using the following parameters: laser power 135−500 W, laser diameter 100 μm, hatch distance 110 μm, scanning speed 300−960 mm/s, and layer thickness of 40 μm. The 3D printing was conducted in the Argon-filled chamber, and the melt pool oxidation was prevented by keeping the oxygen content less than 200 ppm. The chemical composition of 3D printed IN718 substrates analyzed by the energy dispersive spectrometer (EDS) is given in Table 1.

IN718 is a nickel alloy precipitated with different phases such as γ', γ", δ, and MC carbides in the primary γ matrix. The X-Ray Diffraction (XRD) analysis of 3D printed IN718 was conducted before and after polishing for 5 min. The XRD of IN718 substrates was conducted by Cu-K_α radiations operating at 45 kV/200 mA and scanning at a speed of 0.02°. The XRD analysis detected primary matrix γ(Ni-FCC) and secondary γ"(Ni_3Nb-BCT) as major phases in 3D printed IN718, as shown in Fig. 1. The nominal strength of the IN718 is due to the precipitation of the intermetallic phases, such as γ"(Ni_3Nb), which generates coherency strains in the primary γ matrix. Moreover, no phase shift was observed after 5 min of polishing than the XRD of 3D printed IN718.

2.2. Microstructural characterization of 3D printed IN718

Microstructures strongly influence the mechanical properties and electrochemical dissolution characteristics of AM metals and alloys. To reveal microstructures in 3D printed IN718, the substrate was wet grounded with a #1000 grit sandpaper and then polished at 3 A current for 1 min in an electrolyte composed of 20 mL H_2SO_4 mixed in 100 mL CH_3OH. Subsequently, the substrate was ultrasonically washed in ethanol absolute and deionized (DI) water each for 5 min, respectively. The polished substrate was then dried in the open air and immediately etched for 40 s in a waterless Kalling's reagent (100 mL HCl +50 mL C_2H_5OH +5 g $CuCl_2$). The morphology of microstructures was recorded by a laser scanning confocal microscope (LSCM, Keyence VK-X1000) and scanning electron microscope (SEM, 10 ZEISS Merlin).

2.3. Etching process of 3D printed IN718

The 3D printed IN718 substrates were ultrasonically cleaned in DI water and ethanol absolute each for 5 min and dried by air blowing before the IEP experiments. The anisotropic and isotropic etching of 3D printed disc-shaped IN718 substrates (T = 3 mm, D = 15 mm) was conducted in a glass beaker filled with an acidic electrolyte comprising commercial-grade H_2SO_4-97 % mixed in CH_3OH-99.5 %. For anisotropic etching, 1 mL H_2SO_4 was mixed in 100 mL CH_3OH, subsequently written as 1 mL H_2SO_4 electrolyte. Similarly, 20 mL H_2SO_4 electrolyte was prepared for isotropic etching of 3D printed IN718. The IN718 substrate immersed in the electrolyte was connected to the anode of a DC power supply (Keysight E3649A dual output) while the counter electrode was connected to the cathode. The counter electrode used for the disc-shaped 3D printed IN718 substrates was a platinum plate (2 × 2 cm^2), while a curved stainless-steel cathode (T = 2 mm, D = 120 mm, H = 90 mm) was installed to achieve uniform polishing of complex-shaped geometries. The necessary current for anisotropic and isotropic etching was maintained by applying the DC potential difference across the two electrodes separated by 50 mm. All the experiments investigating anisotropic etching, isotropic etching, and IEP surface polishing mechanism, and the polished surface characterizations including roughness, PSD, contour profiles, corrosion resistance, and mechanical tests were conducted on disc-shaped 3D printed IN718 substrates. Simultaneously, SUSTech logos, turbine blade, and the nozzle were polished to prove the

Table 1
Chemical composition of the 3D printed IN718.

Element	Ni	Cr	Fe	Nb	C	Mo	Ti	Mn	Al
(Wt%)	49.06	19.05	20.0	3.95	3.36	2.26	1.04	0.84	0.44

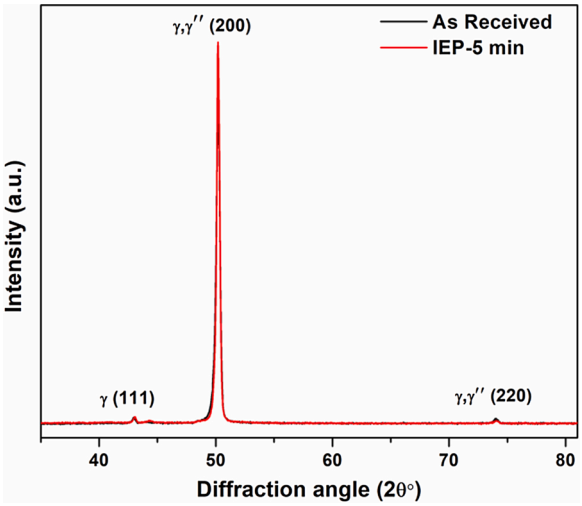

Fig. 1. XRD profiles of 3D printed IN718 substrates, As received and polished at 3 A current for 5 min in 20 mL H_2SO_4 electrolyte.

competency of IEP to process intricate geometries.

2.4. Electrochemical characterization of 3D printed IN718

The potentiodynamic polarization experiments and electrochemical impedance spectroscopy (EIS) of 3D printed IN718 were conducted in a conventional three-electrode reaction cell containing 20 mL H_2SO_4 electrolyte. The reference electrode of Hg/H_2SO_4, cathode (Pt), and 3D printed IN718 substrate immersed in the reaction cell were driven by an electrochemical workstation (CorrTest Instruments-CS350 H) as a potential source. The stability of the working system was realized by recording a stable open circuit potential for 10 min. Subsequently, the EIS tests were conducted over a frequency range of 10^{-3} to 10^5 Hz, while the potentiodynamic polarization response of 3D printed IN718 was recorded by automatically sweeping applied potential from -2.0–3.5 V at a scan rate of 10 mV/s. The potentiodynamic and EIS response of 3D printed IN718 substrates, such as wet grounded with #1000 grit sandpaper and isotropically polished for 5 and 30 min, were compared with the As received substrate. The distance between electrodes and the exposed area of each substrate was kept constant during experiments. The 3D printed IN718 surfaces obtained after potentiodynamic polarization experiments and EIS were also observed by SEM.

2.5. Surface morphology measurements

After IEP for different durations, the evolution of surface topographies was recorded by SEM. The average surface roughness (Sa roughness) was determined by white light interferometer (WLI, CCI HD, Taylor Hobson) over an area of 400 × 400 μm^2 by using a cutoff wavelength of 80 μm, and atomic force microscope (AFM, Bruker Edge) over an area of 10 × 10 μm^2 by using 3rd order surface flattening. The Sa roughness is defined as follows:

$$Sa = \frac{1}{A}\int_A |Z(x,y)|\, dxdy \quad (1)$$

where A is the measurement area, and Z(x,y) is the height of the measured surface from the mean plane. At least five random points from different regions of the substrate were measured for Sa roughness. An indigenous MATLAB code was used to calculate PSD from the surface morphology data acquired by WLI. Besides, the surface contour profiles of 3D printed IN718 were measured by the Profilometer (SURFCOM NEX 031 DX-12).

2.6. Mechanical characterization

Nanohardness and Young's modulus of 3D printed IN718 substrates before and after processing were determined from the nanoindentation load-depth curves. The load-depth curve data include depths relative to the first contact between the indenter and 3D printed IN718 surface. The Hysitron Ti-950 performed the Vickers hardness test by loading, holding, and unloading a 1000 mN force for 10 s each.

3. Results and discussions

3.1. Surface morphology of 3D printed IN718

Schematic of the As received 3D printed IN718 substrate and morphologies at laser scanning tracks, laser scanning track boundaries, and attached powder particles are shown in Fig. 2. Conventionally, laser scanning direction is taken along the y-axis and build direction along the z-axis, as shown in Fig. 2(a). The average width of the crooked laser scanning tracks is approximately 90 μm, as seen from Fig. 2(b), which is shorter than the hatch distance, possibly due to overlapping scanning tracks. In addition to scanning along the y-axis, layer-by-layer deposition of melt pool resulted in metal parts building along the z-axis. Morphologies of the laser scanning tracks and the boundary between two adjoining laser scanning tracks are shown in Figs. 2(c) and (d), respectively. Morphology of the boundary region formed by remelting during succeeding track formation and rapid solidification due to bidirectional temperature gradient is different from laser scanning tracks. According to Liu et al. (2011), an intense heat gradient exists towards the base of the substrate. However, the uppermost layer can also lose heat against the surrounding environment. Therefore, cracks initiated by the rapid solidification and stress are also observed in this region. Micropores are observed approximately on the entire As received IN718 substrate, such as the laser scanning tracks, boundaries, and near the partially melted particles, as shown in Fig. 2(c–e). Zhao et al. (2008) discussed that micropores are caused by the surrounding gas trapping between two consecutive layers, hollow powder particles, and inadequate fusion between layers and laser passes. Shrestha et al. (2019) showed that laser energy density influences pore formation more than scanning speed. That is the reason why SLM manufactured parts suffer from high roughness and asymmetrical mechanical properties. It is to be mentioned that pores formed on the laser track boundaries are irregular in shape, caused by the inadequate fusion between laser passes. In addition, partially melted and unmelted particles attached to the top surface are also observed, as shown in Fig. 2(e and f). Such sites with attached particles are more susceptible to fatigue cracks initiation and deterioration of mechanical and corrosion properties of AM metal components regardless of the stress state, as discussed by Konecná et al. (2016).

3.2. Microstructures on 3D printed IN718

Microstructures observed on the horizontal (perpendicular to the build direction) and vertical cross-sections (in the build direction) of 3D

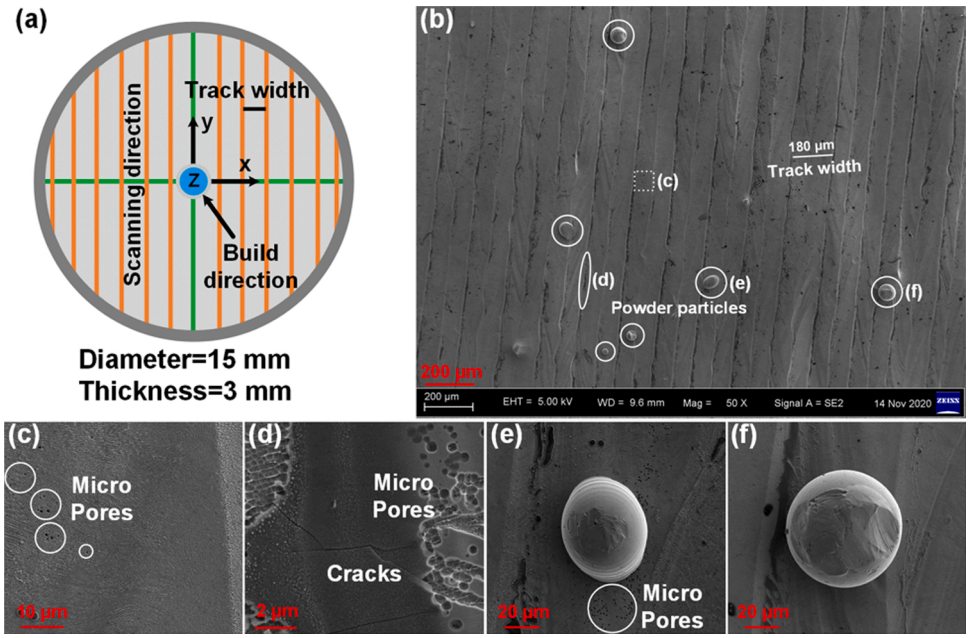

Fig. 2. Schematic (a) and SEM morphologies (b-f) of the As received 3D printed IN718 substrate captured from different regions.

printed IN718 are shown in Fig. 3. The optical micrograph of the horizontal surface shows slightly curved laser scanning tracks with asymmetric widths, as seen from Fig. 3(a). The irregularity in the laser scanning track widths arises due to the remelting of boundaries in succeeding track manufacturing. In contrast to the horizontal surface, melt pool boundaries and cellular dendritic are observed along the build direction, as shown in Fig. 3(b). The cellular dendritic can be seen crossing melt pool boundaries. Cellular dendritic emerge like straight lines, and melt pool boundaries appear in arc-like shape, as marked by the black dotted lines. Cellular dendritic and melt pool boundaries are formed in the heat gradient direction during laser additive manufacturing, as discussed by Liu et al. (2011). Moreover, the distance between dendritic arms is very short, and the width to depth ratio of melt pool boundaries is very high, which might be related to the low energy density, increased scanning speed, and rapid solidification.

Microstructures and grain boundaries observed on horizontal and vertical sections of 3D printed IN718 after chemically etching with Kalling's reagent are shown by the SEM micrographs in Fig. 3(c and d). Different microstructures separated by the grain boundaries are seen on the horizontal surface. Fine hexagonal type equiaxed grains observed on the horizontal surface are shown in the inset of Fig. 3(c). Choi et al. (2017) discussed that equiaxed cellular structures with similar

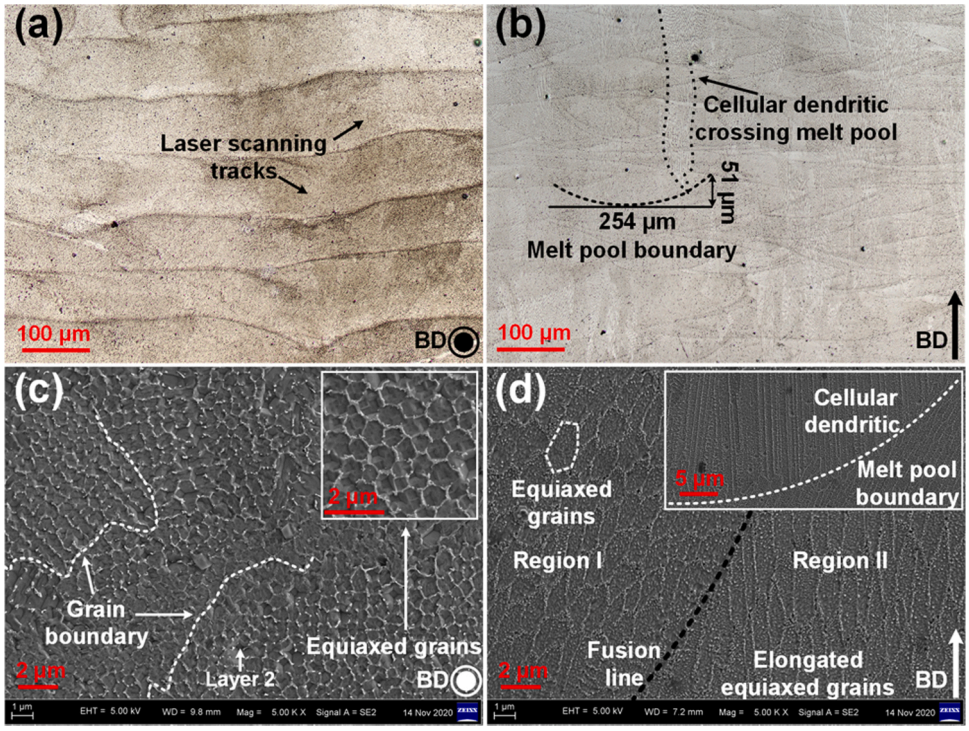

Fig. 3. Microstructures observed on the horizontal and vertical sections of 3D printed IN718 substrate, optical micrographs (a, b), and SEM micrographs (c, d).

crystallographic orientations are formed due to the rapid solidification during AM (10^5–10^7 K/s). In contrast, two distinct regions are observed in the vertical section, as shown in Fig. 3(d). In region I, equiaxed grains are slightly elongated compared to the horizontal section, while the elongation intensifies in region II due to varying heat gradients. Shamsaei et al. (2015) connected the difference in microstructures to the variable heat gradients. The boundaries of cellular structures in 3D printed IN718 are laves phases with a general composition (Ni, Fe, Cr)$_2$(Nb, Mo, Ti). However, laves phase diffraction peaks were not detected by XRD, which might be due to a minimal amount of laves phases than γ-phase, as discussed by Guo et al. (2018b). Epitaxial cellular dendritic formed nearly at 90° to the melt pool boundaries can also be seen in the inset of Fig. 3(d). The epitaxial dendrites and columnar grains are formed along the build direction because of the high-temperature gradient at the liquid-solid interface. In conclusion, irrespective of the major heat gradient along the substrate base, numerous micro heat gradients exist within the bulk resulting in anisotropic microstructural morphologies. It is evident from the difference in grain structures observed on both horizontal and vertical sections of the 3D printed IN718 substrate.

3.3. Etching of 3D printed IN718

Etching can be classified as dry and wet etching, as described by Pal et al. (2021). Wet etching is a chemical-based selective material removing process for the fabrication of high aspect ratio microstructures on the surface of a wafer. The electrolyte selection for wet etching depends on the substrate material. In wet etching, metal is first oxidized by the oxidizing agents in the electrolyte, and then oxidized metal is removed by the metal-ligands (Xia et al., 1996). Wet etching is governed by the diffusion of reactants and products towards and away from the substrate. In contrast, IEP is a generic electrochemical metal polishing technique conducted in a universal electrolyte. In IEP, the oxidizing agent in the electrolyte passivates the substrate, while the applied potential breaks the passive layer, and isotropic etching holes are formed. Both kinetic and diffusion mechanisms govern IEP. However, wet etching and IEP both exhibit isotropic and anisotropic modes depending upon the operating parameters. In metals and alloys, Isotropic etching is the key to realize a smoothly polished surface. The metallic dissolution depends on the electric potential, temperature, and surface energy of the material. Metallic phases in the crystals have different surface energies and orientations, resulting in different dissolution rates and anisotropic etching during kinetic reactions. However, for a uniform density electrolyte, mass transfer current is governed by the electric potential and diffusion coefficient, which is relatively sluggish than the electronic charge transfer and controls the metallic dissolution. Therefore, when the dissolution is diffusion-controlled, the anisotropic etching transforms into isotropic etching, as described by Shaw (1981). The diffusion-controlled dissolution can be realized by increasing the H_2SO_4 concentration in the electrolyte. At room temperature, the viscosity of H_2SO_4 is 20.2 mPa.s (Rhodes and Barbour, 1923) which is very high compared to 0.55 mPa.s for CH_3OH (Kubota et al., 1980). Therefore, increasing H_2SO_4 concentration in the electrolyte significantly improves the electrolyte viscosity, and the metallic ions diffusion towards the bulk electrolyte is suppressed. In addition, the density of SO_4^{-2} acceptor ions and their coordination with the metallic ions considerably increase with the H_2SO_4 concentration, which is desirable to achieve isotropic etching. For electrochemical etching experiments, the 3D printed IN718 substrates were first wet grounded with #1000 grit sandpaper and then electrochemically polished in 20 mL H_2SO_4 electrolyte at 3 A for 60 s. The etching anisotropy of 3D printed IN718 conducted in 1 mL and 20 mL H_2SO_4 electrolytes at 0.3 A for 60 s is shown in Fig. 4. As seen from Fig. 4(a–c), the electrochemical etching conducted in the 1 mL H_2SO_4 electrolyte is anisotropic, where different shapes of the etching holes are attributed to the varying orientation of unlike crystallographic faces relative to the substrate and their odd dissolution when the H_2SO_4 concentration and electrolyte viscosity are very low. In contrast, the electrochemical etching conducted in 20 mL H_2SO_4 electrolyte, keeping the rest of the conditions constant, formed isotropic etching holes, as shown in Fig. 4(d–f). Most of the etching holes in Fig. 4d can be seen merging, whereas hemispherical isotropic etching holes with different diameters can be seen in Fig. 4(e and f). It is to be mentioned that

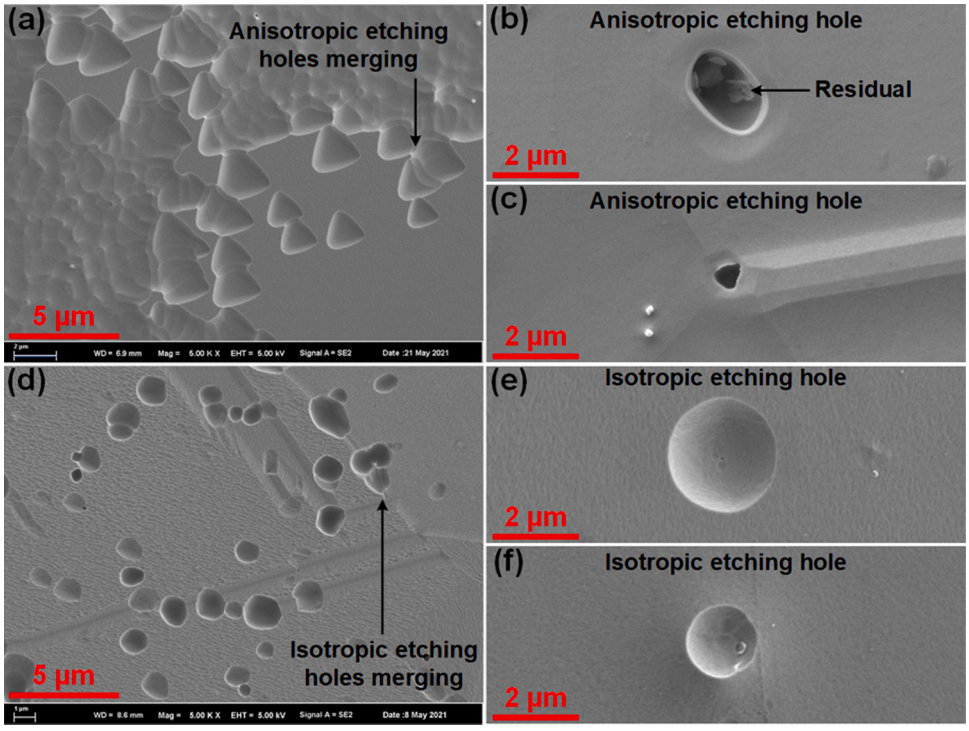

Fig. 4. Electrochemical etching of 3D printed IN718 at 0.3 A current for 60 s, anisotropic etching in 1 mL H_2SO_4 electrolyte (a-c), and isotropic etching in 20 mL H_2SO_4 electrolytes (d-f).

random breakdown of the passivation layer, depending on the initial condition of the substrate and applied voltage, resulted in the variable isotropic etching hole diameters.

3.4. Isotropic etching polishing mechanism of 3D printed IN718

The evolution of the IEP mechanism is shown in Fig. 5. According to the schematic shown in Fig. 5(a), a passive layer (shown in green) is formed at the solid-liquid interface when the metallic substrate is immersed in an acidic electrolyte. The thickness and the electric resistance of the passive layer at different points depend on the initial condition of the substrate. Due to applied potential, the passive layer breaks at weak sites, and isotropic etching holes are generated on the substrate. Isotropic etching holes grow in diameter and merge as polishing progresses. Moreover, the surface roughness during IEP increases with isotropic etching holes formation and then decreases with their merging. The IEP mechanism experimentally observed on As received 3D printed IN718 substrate at 3 A current in 20 mL H_2SO_4 electrolyte is shown in Fig. 5(b–h). After 1 s etching, As received 3D printed IN718 surface was predominantly etched, generating a high density of isotropic holes on the surface, as seen in Fig. 5(b). Compared to the isotropic etching holes in Fig. 4(d), etching holes in Fig. 5(b) are smaller in diameter and higher in density, which is related to the number of breakdown sites and affective etching area at high current. The inset in Fig. 5(b) demonstrates the extensive merging of isotropic etching holes on the substrate. A similar phenomenon is observed on the laser scanning track boundary (Fig. 5c) and partially melted particle attached to the 3D printed IN718 substrate (Fig. 5d and e). After 3 s etching, isotropic etching holes merged, and a new surface was evolved, as shown in Fig. 5(f). Micropores were also observed on the newly developed surface. Shrestha et al. (2019) explained that porosity is one of the challenges in AM caused by the laser operating parameters, also caused by the pre-existing pores in the gas atomized powder, as discussed by Zhao et al. (2008). In addition to the completely dissolved regions, some dark grey regions on the substrate were partially dissolved, as shown in Fig. 5(g). Such areas are formed due to micro-segregation of Ni, Nb, Mo, Cr, etc., during laser solid forming of IN718, as discussed by Guo et al. (2018b). The γ-phase formed due to Nb micro-segregation undergoes preferential electrochemical dissolution because of more negative onset potential and high distortion energy of Nb, as discussed by Guo et al. (2017). Etching up to 10 s improved the surface quality by suppressing the surface porosity. However, certain residual areas, as shown in the inset of Fig. 5(h), required a longer polishing time for uniform smoothening. Anyway, the mechanism of isotropic etching polishing of 3D printed IN718 can be realized regardless of the bulk of γ-phase, laser scanning track boundaries, and powder particles attached to the substrate. Moreover, isotropic etching polishing is necessary for smooth polishing since anisotropic polishing (1 mL H_2SO_4 electrolyte) undergoes asymmetric dissolution of crystallographic phases, and a smoothly polished surface cannot be achieved.

Variation in the Sa roughness and surface morphologies during the IEP mechanism study is shown in Fig. 6. The Sa roughness values given in parentheses in Fig. 6(a) present raw data obtained from AFM. The

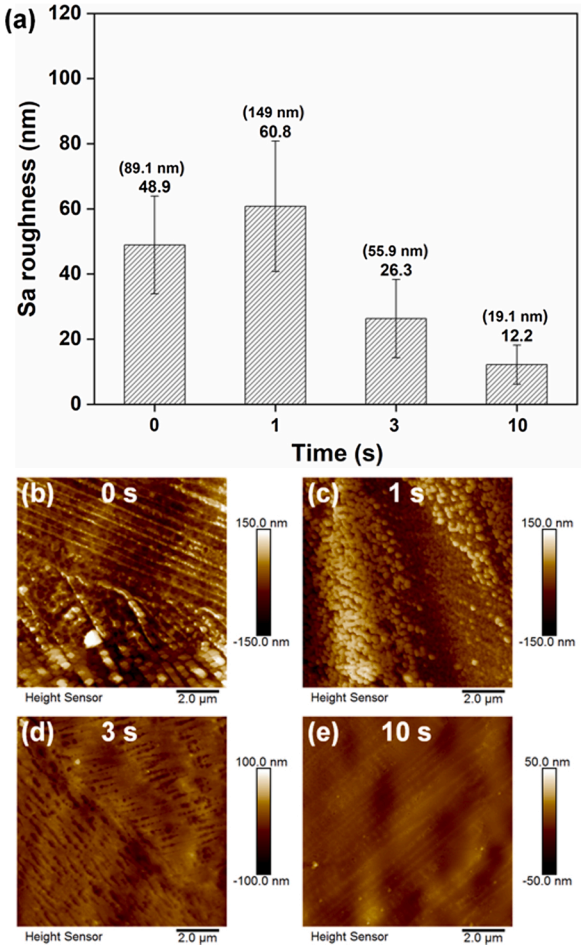

Fig. 6. AFM Sa roughness variation (a), and morphologies of 3D printed IN718 substrates, As received (b) and polished at 3 A current in 20 mL H_2SO_4 electrolytes for 1 (c), 3 (d), and 10 s (e).

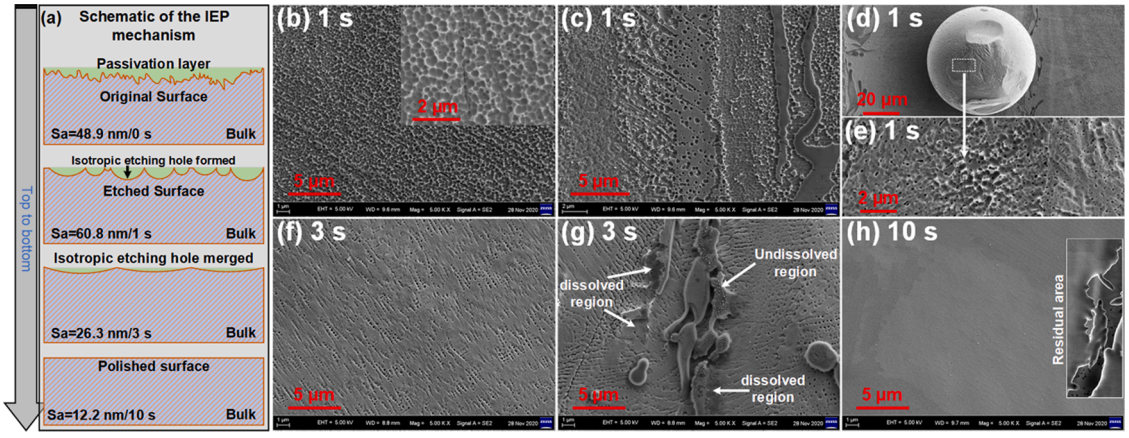

Fig. 5. Isotropic etching polishing mechanism of 3D printed IN718 substrate, (a) schematic, and experimentally investigated at 3 A current in 20 mL H_2SO_4 electrolytes for 1 (b-e), 3 (f-g), and 10 s (h).

initial 48.9 nm Sa roughness of the As received 3D printed IN718 substrate was raised to 60.8 nm after 1 s etching at 3 A in 20 mL H_2SO_4 electrolyte, as shown in Fig. 6(a). An instantaneous rise in the Sa roughness is due to the formation of isotropic etching holes, as shown in Fig. 5(b). After 3 s etching, the isotropic etching holes merged, and a newly polished surface was evolved with Sa roughness reduced to 26.3 nm, as shown in Fig. 6(d). Instantaneous formation and rapid merging of isotropic etching holes are due to the high current breaking the passive layer at weak sites. According to Yi et al. (2020), the surface roughness first increases due to the formation of etching holes and decreases because of their merging. Therefore, the formation and merging of etching holes and the evolution of Sa roughness are consistent with the generic IEP mechanism.

3.5. Isotropic etching polishing characteristics of 3D printed IN718

Inferred from preceding results, IEP of 3D printed IN718 is feasible, and a slightly longer polishing time is required to achieve a uniformly polished surface. Therefore, IEP of 3D printed IN718 was conducted for 3–45 min, and the surface evolution is shown in Fig. 7. In contrast to the polishing for 10 s, no residual polishing areas were observed on the surface after polishing for 3 min. Partially melted particles were removed, and a relatively smooth surface with obvious laser scanning tracks and partially dissolved protrudes on the track boundaries was obtained, as shown in Fig. 7(a). After polishing for 5 min, noticeable edges of laser scanning tracks were dissolved, leaving behind faint impressions of waviness, as shown in Fig. 7(b). IEP for 10 min significantly improved the surface quality by eliminating the laser scanning tracks and waviness. Besides, grain boundaries became evident after 10 min of polishing, as shown in Fig. 7(c). After polishing for 20, 30, and 45 min, grain boundaries on the As received IN718 substrate surface became more distinctive without any height difference, as shown in Fig. 7(d), (e), and (f), respectively.

Improvement in the Sa roughness of 3D printed IN718 substrates after polishing at 3 A in 20 mL H_2SO_4 electrolyte for different durations is determined by WLI, as shown in Fig. 8. The topological WLI profile of the As received 3D printed IN718 in Fig. 8(a) illustrates many protrudes and valleys. Heights of protrudes reduced, and valleys became shallow, while the Sa roughness of As received substrate reduced from 674 nm to 349 nm after polishing for 3 min. Peaks and valleys became indistinct after 5 min and completely disappeared after 10 min of polishing while the Sa roughness was reduced to 84 nm. A rapid decrease in the Sa roughness after a short polishing time was due to the removal of partially melted powder particles. The attached particles are responsible for the high surface roughness and reduced corrosion resistance of the AM IN718 components, as Konecná et al. (2016) discussed. Due to the considerable height difference from the mean plane, a shallow passive layer develops at protruding regions which is easy to break, and protrudes are dissolved rapidly. In addition, the isotropic etching hole formation and merging occurred in this duration. Therefore, intensive improvement in the Sa roughness materialized at the early stage of isotropic polishing. Subsequently, the Sa roughness kept gradually decreasing with increasing polishing duration, and a surface with Sa roughness of 31.5 nm was obtained after polishing for 45 min, as shown in Fig. 8(h). In addition, the Sa roughness values in parentheses present raw data obtained from WLI.

Sometimes, the surface roughness does not adequately differentiate between the two surfaces. For example, two different surfaces having similar features result in the same surface roughness, but these features might be distributed at wider or lower frequency intervals. Therefore, statistical PSD is an appropriate parameter that better describes the spatial features of the surface. The PSD was calculated from the Fourier transform of the WLI roughness data. The PSD function is given as follows:

$$\mathrm{PSD} = \frac{(\mathrm{A}(\nu_i))^2}{\Delta\nu} \tag{2}$$

where $A(\nu_i)$ represents the Fourier amplitude at a given frequency ν_i, and $\Delta\nu$ the incremental change in frequency. The PSD curves in Fig. 9(a) were calculated from the WLI data obtained over an area of 400 × 400 μm^2. After 3 min polishing of 3D printed IN718 substrate, a significant decrease in the PSD was observed over a wide range of spatial frequencies, which is attributed to the IEP mechanism and partially melted particles removing in this duration. A significant improvement in the PSD was observed with extended polishing, but no merging of PSD curves was observed in the low-frequency range. Since low-frequency errors remained predominant on the surface and required extended polishing time, as evident from the decreasing PSD trend. Besides, isotropic polishing realized significant improvement in the high-frequency PSD. Polishing for a longer duration kept improving PSD at all frequencies, though slightly but gradually, and a sort of saturation was observed in the high-frequency range after 30 min of polishing. Variation in the PSD is also consistent with the Sa roughness

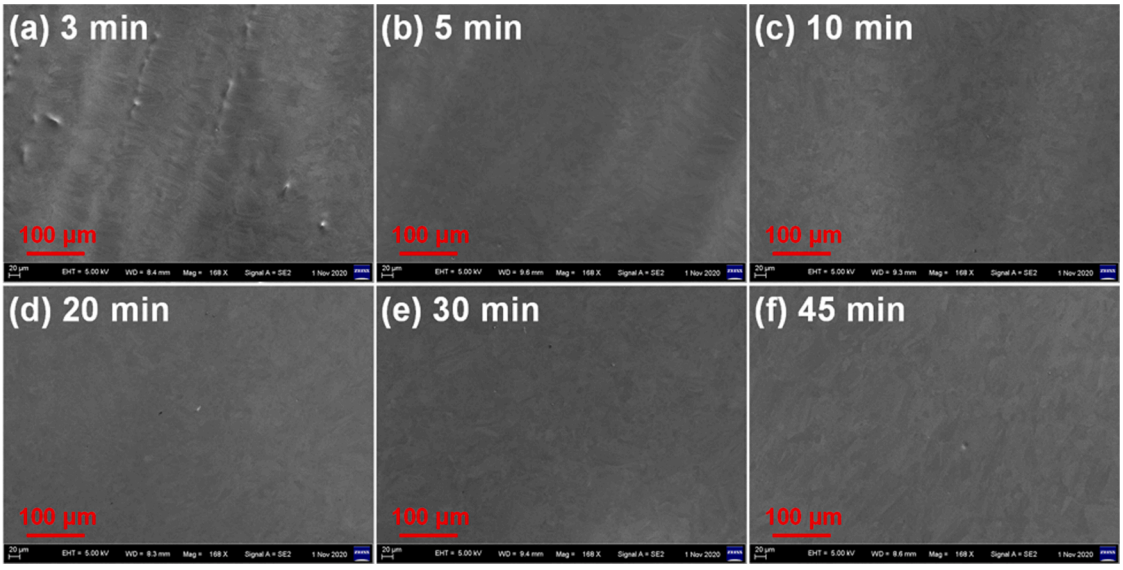

Fig. 7. SEM surface morphologies of 3D printed IN718 substrates polished at 3 A current in 20 mL H_2SO_4 electrolytes for 3 (a), 5 (b), 10 (c), 20 (d), 30 (e), and 45 min (f).

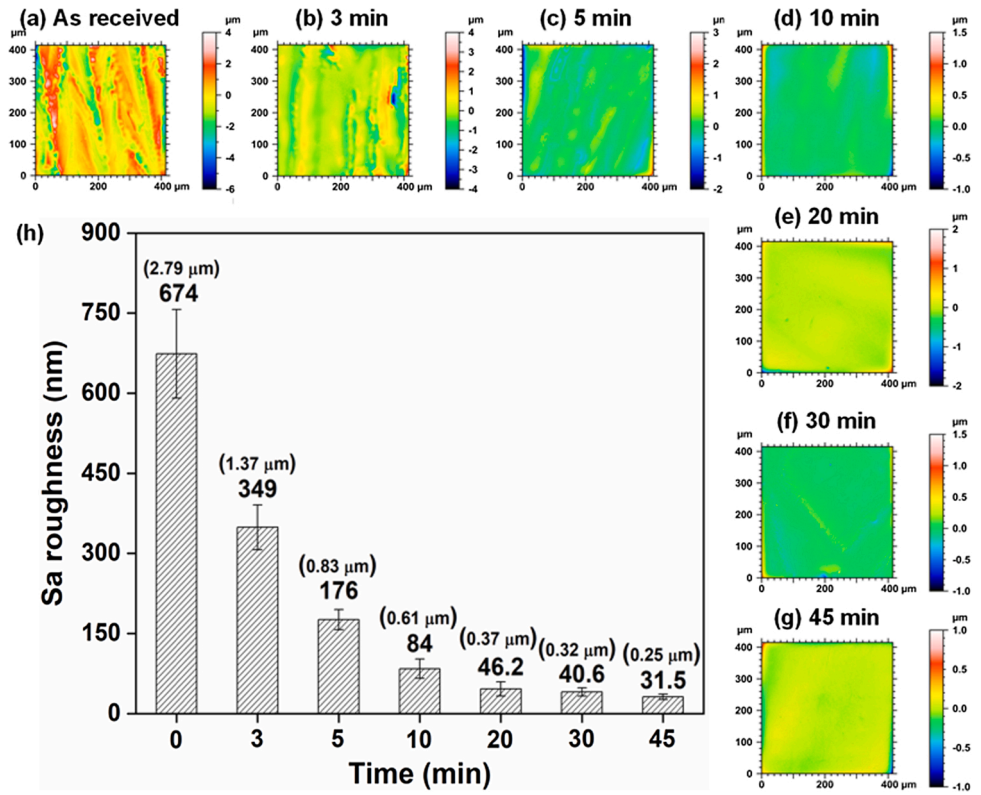

Fig. 8. WLI topological profiles of 3D printed IN718 substrates, As received (a) and polished at 3 A current in 20 mL H_2SO_4 electrolytes for 3 (b), 5 (c), 10 (d), 20 (e), 30 (f), and 45 min (g); and the variation in the Sa roughness (h).

improvement with polishing duration. Hence, it can be concluded that IEP is relatively efficient at removing high-frequency errors. In contrast, low-frequency errors required extended surface processing despite a notable improvement in the surface. The surface morphologies of low-frequency asperities in Fig. 9b and c obtained after 5 and 30 min of IEP are clearly different from high-frequency asperities in Fig. 8c and f.

In addition, the surface line profiles were obtained by using the profilometer, as shown in Fig. 9(d). The line profile recorded from the As received 3D printed IN718 substrate comprises randomly distributed high and low-frequency features. The high-frequency features kept suppressing as polishing progressed and eradicated after polishing for 45 min. Besides, low-frequency asperities were attenuated but could not be removed, even after polishing for 45 min. The line profiles obtained from the profilometer also endorsed the PSD calculated from the WLI data.

Fig. 10 shows 3D printed IN718 substrates isotropically polished up to 45 min. The 3D printed IN718 substrate surface is very rough due to attached powder particles, sharp protruding features, and laser scanning tracks. The 3D printed IN718 substrate looks very dull in contrast to the isotropically polished substrates. After polishing for 3 min, the surface became shiny and kept improving with further polishing. Besides, no significant edge rounding was observed up to 10 min of polishing. After 20 min, prominent edge rounding was observed, which became severe after 45 min. Furthermore, the surface became flat and shiny due to the dissolution of protrudes and valleys, compared to the As received 3D printed IN718 substrate. It is to be mentioned that a Teflon holder covering the backend of the polishing substrate prevented its polishing and fixed the substrate position relative to the cathode. Therefore, the front face of the substrate was polished exclusively.

The MRR of 3D printed IN718 is calculated from the difference in mass before and after polishing. The variation in the MRR with increasing current and electrolyte concentration is shown in Fig. 11. As seen from Fig. 11(a), the MRR linearly rises with current, and the highest value of MRR (2.42 mm^3/min) corresponds to the maximum current (3A). A linear relation between MRR and rising current indicates rapid dissolution as a result of high ion mobility. Fig. 11(b) shows the variation in the MRR with electrolyte concentration and increasing current. The low electrical conductivity of 1 mL H_2SO_4 electrolyte allowed electric current only up to 1 A, so no data for 1 mL electrolyte could be acquired at 1.5 A current. The MRR reduced with the electrolyte concentration at a constant current, which became more evident at a relatively higher current (1.5 A). At higher H_2SO_4 concentration in the electrolyte, the diffusion of metal ions is suppressed, while the electrochemical reaction between by-products also impedes metal dissolution, thus reducing the MRR with increasing electrolyte concentration.

3.6. Anodic polarization of 3D printed IN718

The anodic polarization response of 3D printed IN718 substrates, As received, wet grounded with #1000 grit sandpaper, and polished for 5 and 30 min, are shown in Fig. 12. The polarization curves sketched similar cathodic, anodic, passive, and transpassive regions in 20 mL H_2SO_4 electrolyte. Analysis of the Tafel region showed that the corrosion potential (V_{corr}) of 3D printed IN718 substrates increased, and corrosion current (I_{corr}) decreased after surface treatment, as shown in the inset of Fig. 12. The parameters obtained from the analysis of the Tafel region are given in Table 2. For example, the V_{corr} of 3D printed IN718 increased from -0.59 V to -0.44 V after wet grounding. The V_{corr} increased to -0.37 V when the As received 3D printed IN718 substrate was polished for 5 min. However, after 30 min of polishing, the V_{corr} slightly decreased to -0.38 V. According to Ma et al. (2018), more noble V_{corr} represents higher corrosion resistance. The I_{corr} showed an inverse tendency and dropped with the surface treatment of 3D printed IN718 substrate. The I_{corr} significantly reduced from 95 µA to 69 µA after the wet grounding of As received 3D printed IN718 substrate. With the IEP of As received 3D printed IN718, the I_{corr} first decreased to 39 µA after polishing for 5 min and then increased to 58 µA with polishing duration extending to 30 min. According to Faraday's law, the corrosion rate is

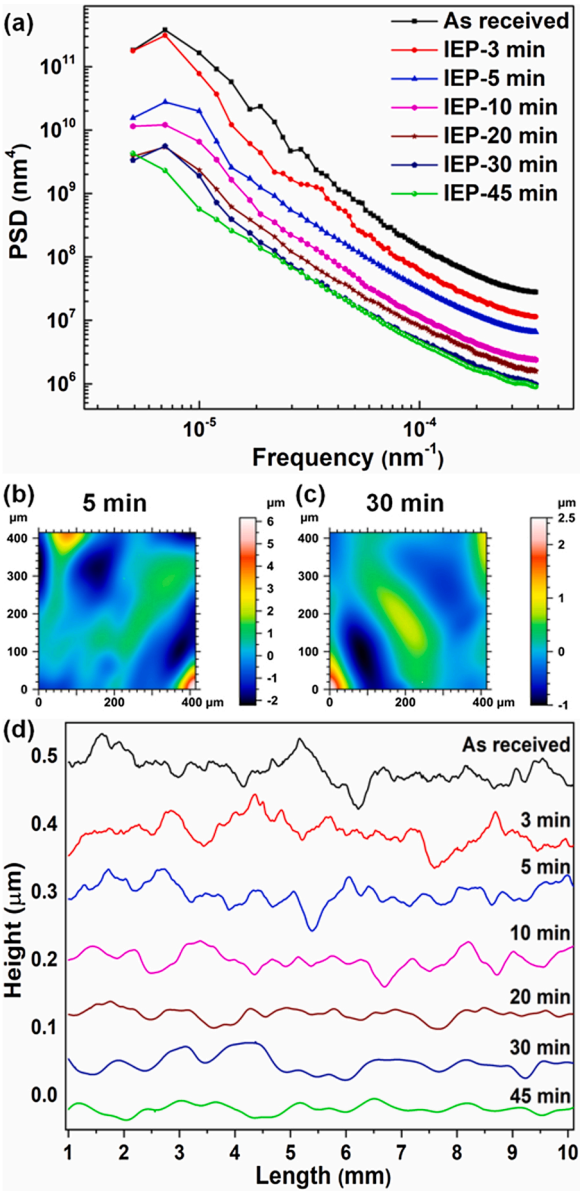

Fig. 9. 3D printed IN718 substrates, As received and polished at 3 A current for 3 to 45 min in 20 mL H_2SO_4 electrolytes, PSD (a), morphologies of low-frequency asperities after polishing for 5 min (b) and 30 min (c), and line profiles (d).

positively related to the I_{corr}, as Shi et al. (2014) discussed.

The surface morphologies of 3D printed IN718 substrates before and after anodic polarization experiments are shown in Fig. 13. The surface quality of 3D printed IN718 and wet grounded substrates are relatively inferior to the isotropically polished substrates. The surface corrosion resistance is susceptible to porosity, attached particles, and defects caused by grounding, as discussed by Konecná et al. (2016). In contrast, after polishing for 5 min, the 3D printed IN718 surface became very smooth. The Sa roughness was significantly reduced due to the dissolution of laser scan boundaries and the removal of attached particles. Therefore, the corrosion resistance improved substantially with the surface quality. Although the corrosion resistance of the substrate polished for 30 min slightly deteriorated, it was still better than the As received and grounded 3D printed IN718 substrates. If we closely observe Fig. 13(d), the preferentially dissolved regions are similar to the equiaxed microstructures (Section 3.2) marked on the horizontal surface of 3D printed IN718. In additively manufactured IN718, these regions are formed due to Nb micro-segregation, as discussed by Guo et al. (2018b). Therefore, it is believed that the relatively lower corrosion resistance of the substrate polished for 30 min is due to the preferential dissolution of the Nb-rich phases, which generated active corrosion sites with poor resistance. Guo et al. (2017) found that Nb-rich phases dissolve more rapidly due to higher lattice distortion energy and more negative potential. In addition, atoms located on phase boundaries have high free energy, promoting rapid dissolution of Nb-rich phases. Sutow (1980) found a similar tendency of corrosion potential after ECP of 316 L stainless steel for different durations. A similar sequence of corrosion potential, current, and corrosion rate was reported by Hassan and Ghany (2017) after ECP of 316 L stainless steel. Although the 3D printed IN718 substrates showed no pitting signs after anodic polarization experiments, the surface was not smooth, and equiaxed microstructures were exposed, as shown in Fig. 13(a'–d').

Further analysis of Fig. 12 shows the evolution of the primary passivation region. According to Sikora and Macdonald (2002), the active dissolution of Ni from the alloy resulted in the formation of NiO, which is responsible for the primary passivation of IN718 in acidic electrolytes. The passive regions of all the curves are similar. The passive current (I_{pass}) given in Table 2 is the average of the highest and lowest current recorded in the passive region. The I_{pass} first decreased with surface processing and then increased after 30 min of polishing. At a relatively higher voltage, an immediate fluctuation in the current density is observed due to the second passivation. In acidic electrolytes, the secondary passivation of IN718 is commonly associated with the anodic reactions resulting in the formation of NiO_2, as discussed by Chaudhary and Singh. (1993). Further increase in the applied voltage rapidly increased the current density due to the breakdown of the passive layer and the onset of the transpassive region. The current density became independent of the applied voltage in this region, and the reaction became mass controlled.

3.7. EIS of 3D printed IN718

The Nyquist plots of 3D printed IN718 substrates, As received, wet grounded with #1000 grit sandpaper, and polished for 5 and 30 min are compared in Fig. 14(a). The Nyquist plot showed a different response at high and low frequencies. In fact, the electrochemical dissolution of metallic electrodes is governed by charge transfer and mass-controlled processes. Semicircle at high frequencies conceals charge transfer resistance (R_{ct}) of kinetically controlled processes. The straight line at low frequencies represents Warburg impedance (W_s), realizing the diffusion of reaction products towards or away from the surface, as discussed by Skotheim et al. (1998).

The Nyquist plot of the As received substrate is different from grounded and polished samples. At high frequencies, the former has a semicircle with the shortest diameter, followed by a straight line at low frequencies. The semicircle diameter accounts for the degradation rate, and a short diameter indicates less effective anti-corrosion film with low R_{ct}. A short semicircle diameter at high frequencies speculates a rapid kinetically controlled process compared with the sluggish diffusion represented by a straight line at low frequencies. The kinetic and diffusion-controlled processes occur in series, and the slower of them is the rate-determining step. The Nyquist plot of grounded 3D printed IN718 substrates is similar to polished for 30 min, where the latter shows slightly higher R_{ct}. As discussed, prolonged polishing resulted in the preferential dissolution of laves phases and generated active corrosion sites. However, the R_{ct} is highest for 3D printed IN718 substrate polished for 5 min, as evident from the largest semicircle. The improved charge transfer resistance is due to the removal of attached particles, reduced surface roughness, and the development of a thick passivation layer that blocks the electron penetration. Similar trends of the Nyquist plot and the variation in the corrosion resistance of ECP processed 316 L stainless steel have been reported by Hassan and Ghany (2017).

The impedance data were further quantified by fitting the experi-

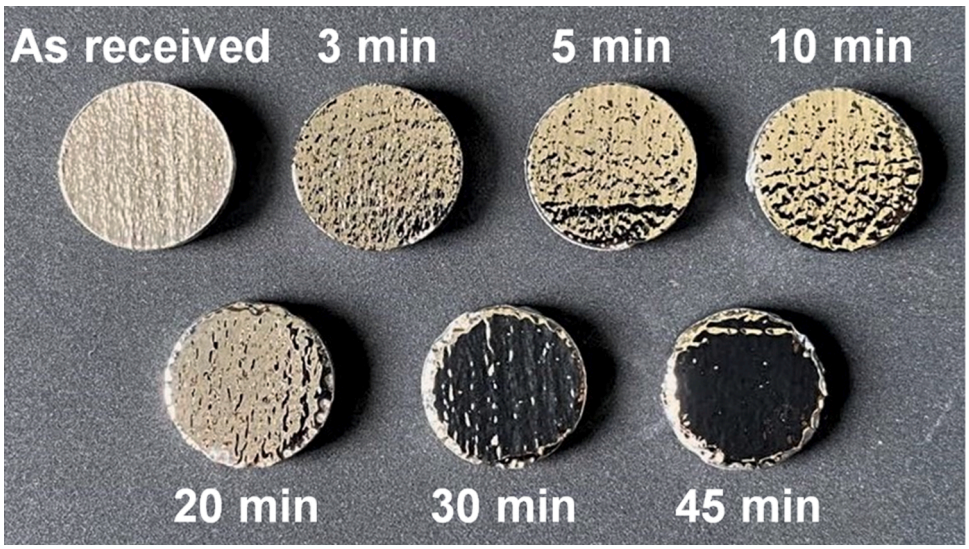

Fig. 10. Images of 3D printed IN718 substrates, As received and polished at 3 A current for 3 to 45 min in 20 mL H_2SO_4 electrolytes.

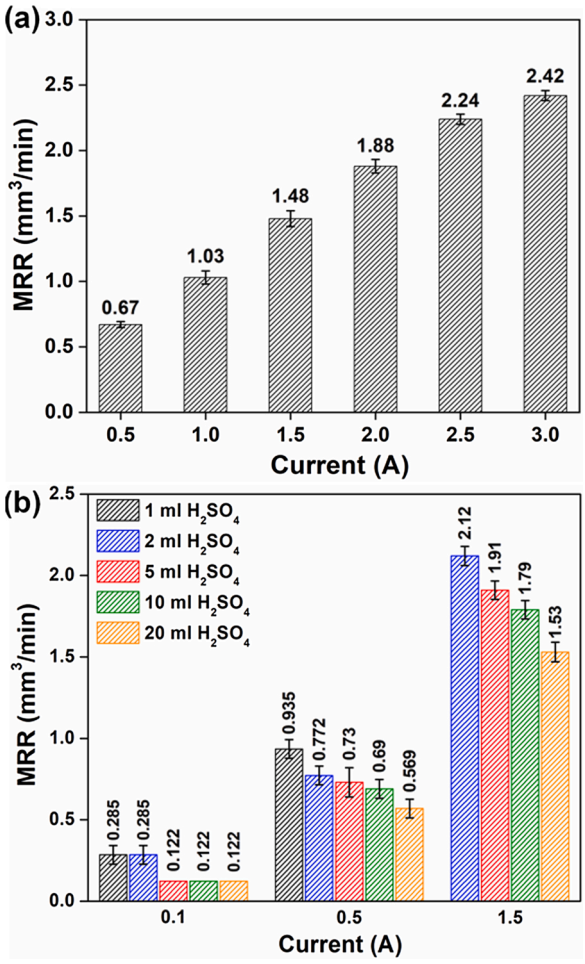

Fig. 11. Material removal rate of 3D printed IN718, IEP for 300 s in 20 mL H_2SO_4 electrolyte with increasing current (a), and IEP for 60 s with increasing current and H_2SO_4 concentration (b).

mental Nyquist plots using an equivalent circuit model shown in Fig. 14 (b). This equivalent circuit model has already been used to interpret corrosion parameters of the passive film by Sánchez-Tovar et al. (2015). The fitting parameters are given in Table 3. Solid black fitting lines in

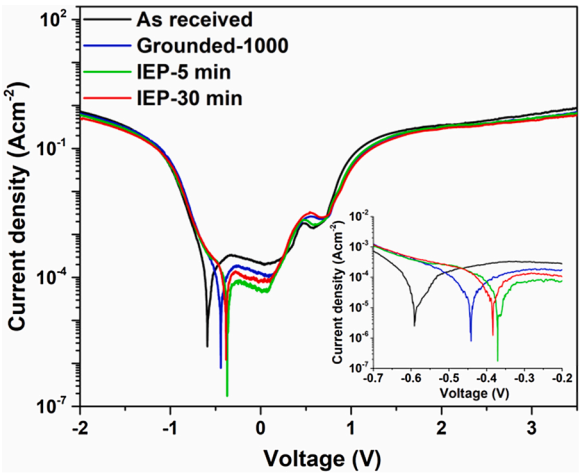

Fig. 12. Anodic polarization curves of 3D printed IN718 substrates, As received, wet grounded, and polished at 3 A current for 5 and 30 min in 20 mL H_2SO_4 electrolytes.

Table 2
Parameters obtained from the analyses of Tafel regions in anodic polarization curves.

Substrate	V_{corr} (V)	I_{corr} (μA)	I_{pass} (μA)
As received	−0.59	95	268
Grounded-1000	−0.44	69	147
IEP-5 min	−0.37	39	62
IEP-30 min	−0.38	58	108

Fig. 14(a) show excellent agreement with experimental data. Labeled in the equivalent circuit model, R_s presents electrolyte resistance, R_1 passive film resistance, R_{corr} polarization resistance, R_1 and R_{corr} collectively account for R_{ct}, and W_s Warburg element. Constant phase elements CPE1 and CPE2 belonging to passive film and double layer are accountable for modeling the inhomogeneity of the electrode, as discussed by Compère et al. (1993). The impedance Z_{CPE} is defined as follows:

$$Z_{CPE} = \frac{1}{C(j\omega)^n} \quad (3)$$

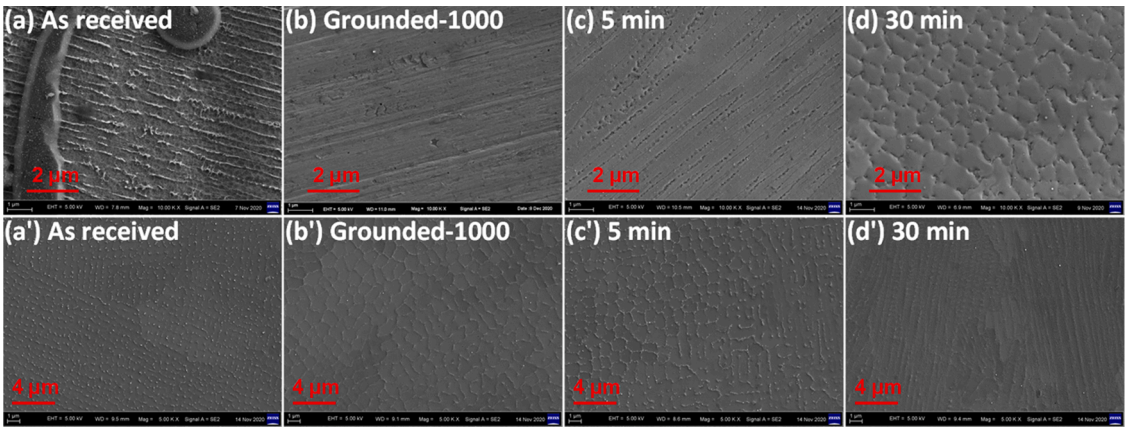

Fig. 13. SEM morphologies of 3D printed IN718 substrates, As received, wet grounded, and polished at 3 A current for 5 and 30 min in 20 mL H_2SO_4 electrolytes, before (a, b, c, d), and after (a', b', c', d') anodic polarization experiments.

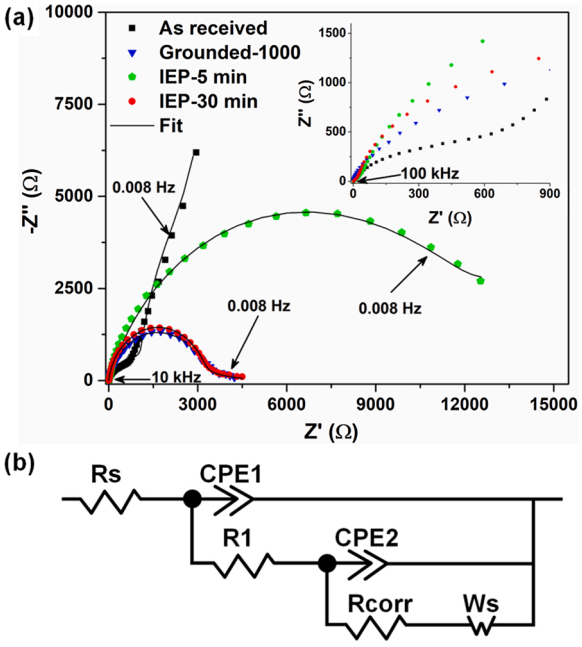

Fig. 14. Nyquist plots of 3D printed IN718 substrates As received, wet grounded, and polished at 3 A current for 5 and 30 min in 20 mL H_2SO_4 electrolytes (a) and Equivalent circuit model (b).

where C is a constant, j an imaginary number, ω angular frequency, and the depression parameter n=-1, 0, 1 respectively describe the ideal inductor, resistor, and capacitor.

There are two different time constants, (CPE1-T) at high frequency and (CPE2-T) at low frequency, used in the fitting process. At high frequency, CPE1-T accounts for passive film capacitance in pore-free regions and the ionic resistance of the pore areas. Pores or defects in the passive layer allow the passage of electrolyte towards the substrate and promote CPE2-T. The second time constant accounts for the substrate response against the pores in the viscous layer. Besides, the values of CPE2-P are greater than CPE1-P, showing better capacitance of the inner layer than the outer barrier layer. R_{corr} is the charge transfer resistance of the porous layer, which increased with the surface treatment. Similarly, the sum of R_{corr} and R_1 increased after surface processing, with the highest for a substrate polished for 5 min, as evident from the largest Nyquist plot diameter. In addition, the significantly higher value of R_1 describes the dominant protective role by the passive layer compared with R_{corr}, as discussed by Fernández-Domene et al. (2012). W_s-R_w shows that the substrate treated for 5 min by IEP has the least permeable passive film. In short, a more compact and uniform passive film was formed on IEP processed substrates, which shows improved corrosion resistance compared with the As received and grounded substrates.

3.8. Mechanical properties of 3D printed IN718

The mechanical properties of 3D printed IN718 substrates, wet grounded and polished for 5 and 30 min, are compared with the As received sample. The nanoindentation curves, hardness, and Young's modulus of all the substrates are shown in Fig. 15. Compared with the As received 3D printed IN718 substrate, the penetration depth of the indenter first decreased for the grounded substrate and then increased for polished samples, as shown in Fig. 15(a). The hardness and Young's modulus exhibited a similar trend. After grounding As received 3D printed IN718 substrate, the hardness increased from 5.06 to 6.81 GPa and Young's modulus from 201 to 219 GPa, as shown in Figs. 15(b) and (c), respectively. Xin et al. (2016) demonstrated that the grounding process induces plastic deformation of the surface and increases residual stress, ultimately improving the mechanical properties. On the other hand, nanoindentation depth, hardness, and Young's modulus slightly decreased after isotropic etching polishing. Chlebus et al. (2015) stated that high laser energy density and rapid cooling induce stress on the As received substrates, while electrochemical based polishing of metals releases the residual stress due to the removal of different phases. For example, the hardness and Young's modulus of 3D printed IN718 substrate polished for 30 min is minimal, attributed to the dissolution of brittle and hard laves phase responsible for surface hardness. Guo et al. (2017) discussed that the boundaries of microstructures in the 3D

Table 3
Parameters of Nyquist plots fitting experimental data by using the equivalent circuit.

Substrate	R_s (Ωcm^2)	R_{corr} (Ωcm^2)	R_1 (Ωcm^2)	CPE1-T (s)	CPE1-P	CPE2-T (s)	CPE2-P	W_s-R_w (Ωcm^2)	W_s-T (s)	W_s-P
3D printed	1.82	12	1800	0.00051	0.75	0.0032	1.25	35050	200	0.61
Grounded-1000	0.74	20	3280	0.00046	0.85	0.02	1.8	5850	100	1.82
IEP-5 min	1.86	100	12800	0.00020	0.78	0.01	0.73	45350	225	1.3
IEP-30 min	2.83	30	3290	0.00027	0.91	0.011	1.7	7200	100	1.92

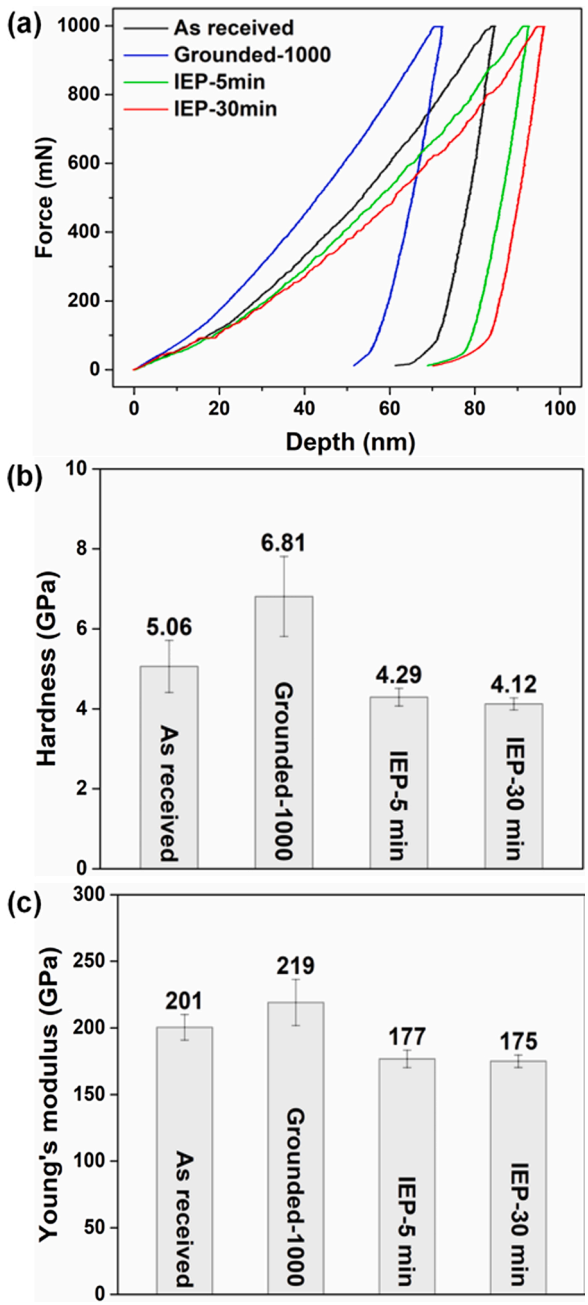

Fig. 15. Nanoindentation curves (a), hardness (b), and Young's modulus (c) of 3D printed IN718 substrates, As received, wet grounded, and polished at 3 A current for 5 and 30 min in 20 mL H_2SO_4 electrolytes.

printed IN718 are made of laves phases. And sites with laves phases are more susceptible to crack initiation and destroying the mechanical properties of the material. In addition, the dissolution of γ and γ" also reduced the surface hardness of the isotropically polished 3D printed IN718 substrates. Typically, the fatigue performance of AM parts is more dominated by the surface finish rather than the microstructures and mechanical properties (Greitemeier et al., 2016). Therefore, a slight decrease in the microhardness can be a valuable tradeoff with the improved corrosion resistance of IN718 after IEP, which can significantly improve device performance.

3.9. IEP of complex 3D printed IN718 parts

The competency of IEP was further certified by polishing different 3D printed IN718 complex geometries, such as SUSTech logos, turbine blade, and nozzle, as shown in Fig. 16. In contrast to the As received complex geometries (Fig. 16a), isotropic polishing for 5 min at 3 A current in 20 mL H_2SO_4 electrolytes significantly improved their surface quality (Fig. 16b). Accordingly, 3D printed complex parts became very shiny, and their surfaces became reflecting. In addition, the SEM morphologies of an alphabet "e" from As received and polished logo 1 are shown in Fig. 16(c and d). The alphabet on logo 1 was finely polished with no significant damage to thin walls, as shown in Fig. 16(c1 and d1). Besides, Sa roughness of these complex geometries was measured using WLI. As evident from Fig. 17, protruding regions became flat, and up to 76 % improvement in the Sa roughness was recorded after polishing for 5 min. Therefore, the developed technology can be a potential applicant in futuristic industries seeking complex geometries with finely polished surfaces and improved corrosion properties.

4. Conclusions

In this study, isotropic etching polishing of 3D printed IN718 at 3 A in 20 mL H_2SO_4 electrolyte is proposed. Microstructures in the As received 3D printed IN718 were exposed by the chemical etching. The anisotropic etching was transformed into isotropic etching, and the latter was further realized as the polishing mechanism of 3D printed IN718. Subsequently, the polishing characteristics and surface roughness evolution with polishing duration, material removal rate, and electrochemical and mechanical properties of 3D printed IN718 substrates with different treatments were determined. The key findings are:

(1) Crystallographic phases in 3D printed IN718 have different surface energies and dissolution rates that result in anisotropic electrochemical etching. Electrochemical isotropic etching of 3D printed IN718 can be realized under the diffusion-controlled dissolution, which is achieved via increasing highly viscous H_2SO_4 concentration in CH_3OH. Isotropic etching holes formation and merging on 3D printed IN718 first increased the surface roughness and then instantaneously decreased, which is consistent with the IEP mechanism.
(2) Besides the IEP mechanism realizing at the early stage of polishing, certain partially dissolved or undissolved areas require additional time for atomic polishing. Such as the initial 674 nm Sa roughness of 3D printed IN718 substrate was reduced to 31.5 nm after 45 min of polishing.
(3) The MRR increasing with current indicates a more efficient IEP. Besides, a negligible reduction in MRR becomes prominent with increasing current and electrolyte concentration.
(4) Compared to the grounded and As received 3D printed IN718 substrates, IEP significantly improved the corrosion resistance, which is slightly influenced by the IEP duration. Besides, wet grounding and IEP have different effects on the surface mechanical properties, which slightly decreased after IEP relative to the As received 3D printed IN718 substrate.

The 3D printed IN718 complex parts, such as SUSTech logos, turbine blade, and nozzle, were also polished, and the Sa roughness was improved up to 76 %. Current findings opened new windows for IEP in futuristic mechanical industries seeking complex geometries with inner features.

CRediT authorship contribution statement

Khan Muhammad Ajmal: Data curation, Methodology, Writing - original draft. **Rong Yi:** Data curation, Methodology. **Zejin Zhan:** Data curation, Methodology. **Jianwei Ji:** Data curation, Methodology. **Linfeng Zhang:** Data curation, Methodology. **Hui Deng:** Conceptualization, Supervision, Writing - review & editing.

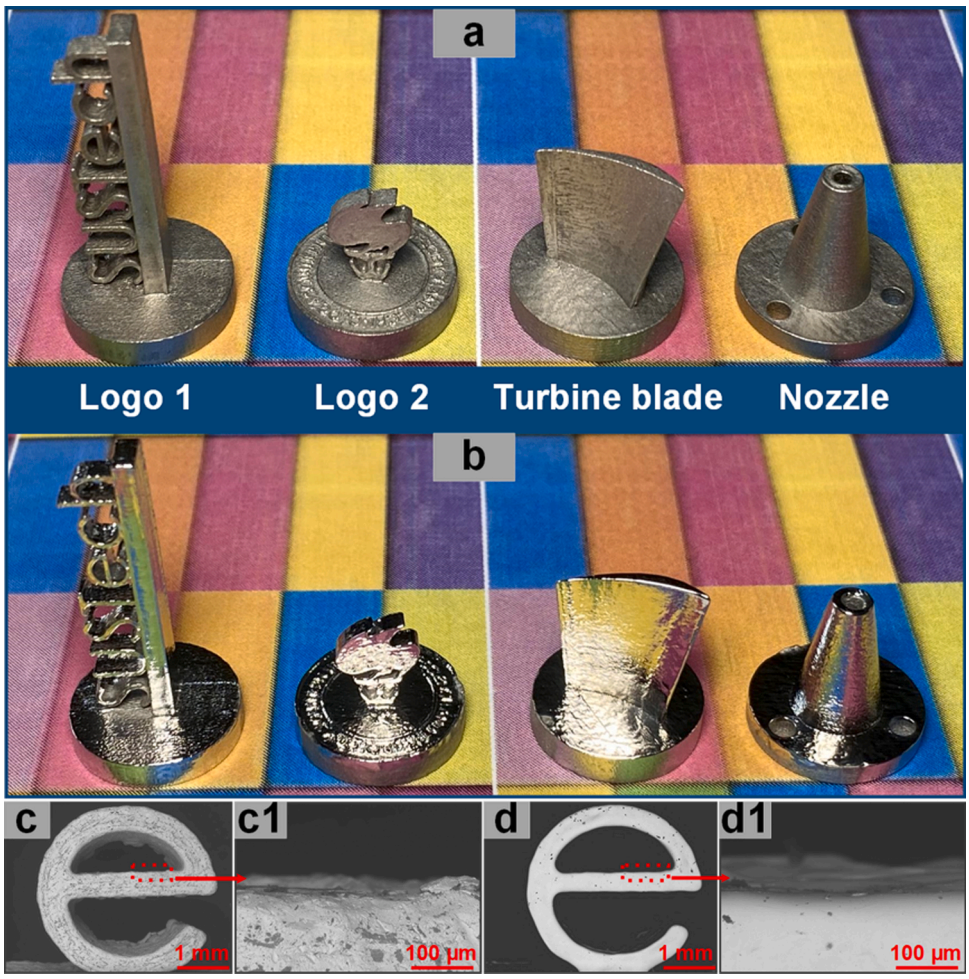

Fig. 16. 3D printed IN718 complex parts and SEM morphologies As received (a, c, and c1), and after polishing for 5 min in 20 mL H_2SO_4 electrolytes (b, d, and d1).

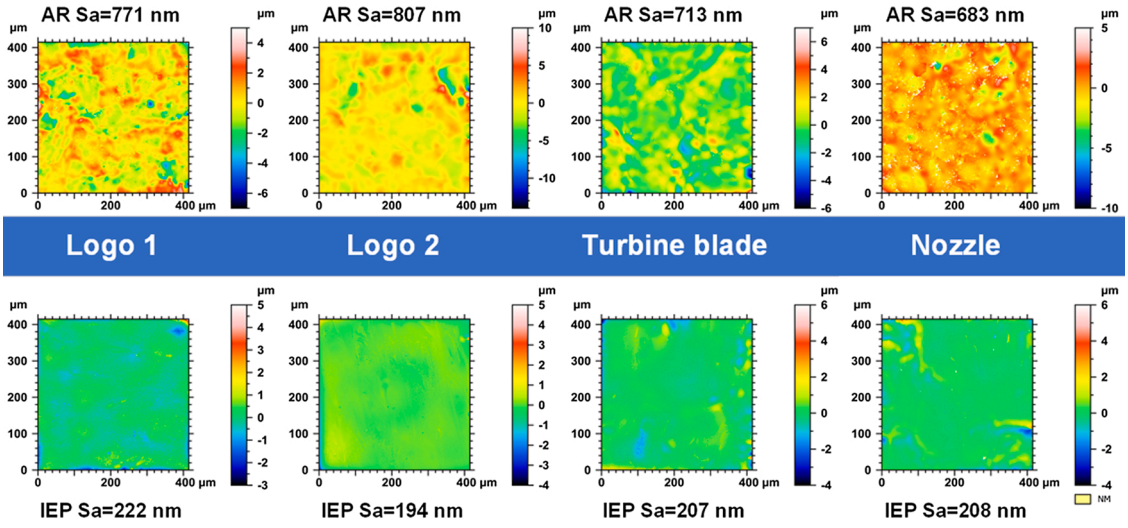

Fig. 17. WLI profiles of 3D printed IN718 complex parts before and after polishing at 3 A for 5 min in 20 mL H_2SO_4 electrolytes.

Declaration of Competing Interest

The authors report no declarations of interest.

Acknowledgments

This project is supported by National Natural Science Foundation of China (Grant No. 52035009, 52005243), the research fund for International Cooperation (GJHZ20180928155412525), and the Shenzhen High-level Innovation and Entrepreneurship Fund

(KQTD20170810110250357) from the Science and Technology Innovation Committee of Shenzhen Municipality, Shenzhen, China. The authors acknowledge the assistance of SUSTech Core Research Facilities.

References

Baicheng, Z., Xiaohua, L., Jiaming, B., Junfeng, G., Pan, W., Chen-nan, S., Muiling, N., Guojun, Q., Jun, W., 2017. Study of selective laser melting (SLM) Inconel 718 part surface improvement by electrochemical polishing. Mater. Des. 116, 531–537. https://doi.org/10.1016/j.matdes.2016.11.103.

Chaudhary, R.S., Singh, A., 1993. Transpassive anodic dissolution of nickel in sulphuric acid. Brit. Corros. J. 28, 227–230. https://doi.org/10.1179/000705993798318470.

Chlebus, E., Gruber, K., Kuznicka, B., Kurzac, J., Kurzynowski, T., 2015. Effect of heat treatment on the microstructure and mechanical properties of Inconel 718 processed by selective laser melting. Mater. Sci. Eng. A 639, 647–655. https://doi.org/10.1016/j.msea.2015.05.035.

Choi, J.-P., Shin, G.-H., Yang, S., Yang, D.-Y., Lee, J.-S., Brochu, M., Yu, J.-H., 2017. Densification and microstructural investigation of Inconel 718 parts fabricated by selective laser melting. Powder Technol. 310, 60–66. https://doi.org/10.1016/j.powtec.2017.01.030.

Compère, C., Fréchette, É., Ghali, E., 1993. The corrosion evaluation of painted and artificially damaged painted steel panels by AC impedance measurements. Corros. Sci. 34, 1259–1274.

De Giorgi, C., Furlan, V., Demir, A.G., Tallarita, E., Candiani, G., Previtali, B., 2016. Laser micro-polishing of stainless steel for antibacterial surface applications. Procedia CIRP 49, 88–93. https://doi.org/10.1016/j.procir.2015.07.055.

Fang, F., 2020. Atomic and close-to-atomic scale manufacturing: perspectives and measures. Int. J. Extrem. Manuf. 2, 030201 https://doi.org/10.1088/2631-7990/aba495.

Fernández-Domene, R.M., Blasco-Tamarit, E., Garcia-Garcia, D.M., Garcia-Anton, J., 2012. Thermogalvanic corrosion of Alloy 31 in different heavy brine LiBr solutions. Corros. Sci. 55, 40–53. https://doi.org/10.1016/j.corsci.2011.10.001.

Greitemeier, D., Dalle Donne, C., Syassen, F., Eufinger, J., Melz, T., 2016. Effect of surface roughness on fatigue performance of additive manufactured Ti–6Al–4V. Mater. Sci. Technol. 32, 629–634. https://doi.org/10.1179/1743284715Y.0000000053.

Guo, P., Lin, X., Xu, J., Li, J., Huang, W., 2017. Electrochemical removal of different phases from laser solid formed inconel 718. J. Electrochem. Soc. 164, E151. https://doi.org/10.1149/2.0951707jes.

Guo, P., Lin, X., Ren, Y., Xu, J., Li, J., Zhang, Y., Chen, J., Huang, W., 2018a. Microstructure and electrochemical anodic behavior of Inconel 718 fabricated by high-power laser solid forming. Electrochim. Acta 276, 247–260. https://doi.org/10.1016/j.electacta.2018.04.186.

Guo, P., Lin, X., Zhang, Y., Li, J., Xu, J., Ren, Y., Liu, J., Yang, H., Huang, W., 2018b. Distinction in anodic dissolution behavior of inconel 718 prepared by different forming technologies. J. Electrochem. Soc. 165, E546. https://doi.org/10.1149/2.1071811jes.

Han, P., 2017. Additive design and manufacturing of jet engine parts. Engineering 3, 648–652. https://doi.org/10.1016/J.ENG.2017.05.017.

Hassan, N., Ghany, N.A.A., 2017. Science, and technology, corrosion of biomaterials: anodic treatment and evaluation of 316L stainless steel in simulated body fluid. Corros. Eng. Sci. Technol. 52, 267–275. https://doi.org/10.1080/1478422X.2016.1267932.

Jacquet, P.A., 1936. On the anodic behavior of copper in aqueous solutions of orthophosphoric acid. Trans. Electrochem. Soc. 69, 629–655.

Kaynak, Y., Tascioglu, E., 2019. Post-processing effects on the surface characteristics of Inconel 718 alloy fabricated by selective laser melting additive manufacturing. Prog. Addit. Manuf. 1–14. https://doi.org/10.1007/s40964-019-00099-1.

Khan, M.A., Yi, R., Zhan, Z., Ji, J., Zhang, X., Deng, H., 2021. Highly efficient smoothing of Inconel 718 via electrochemical-based isotropic etching polishing. Precis. Eng. 71, 119–129. https://doi.org/10.1016/j.precisioneng.2021.03.005.

Konecná, R., Kunz, L., Nicoletto, G., Baca, A., 2016. Fatigue crack growth behavior of Inconel 718 produced by selective laser melting. Frattura integr. Strutt. 10, 31–40.

Kubota, H., Tsuda, S., Murata, M., Yamamoto, T., Tanaka, Y., Makita, T., 1980. Specific volume and viscosity of methanol-water mixtures under high pressure. Rev. Phys. Chem Jap. 49, 59–69.

Li, Y., Zhang, Z., Guan, Y., 2020. Thermodynamics analysis and rapid solidification of laser polished Inconel 718 by selective laser melting. Appl. Surf. Sci. 511, 145423 https://doi.org/10.1016/j.apsusc.2020.145423.

Liu, F., Lin, X., Yang, G., Song, M., Chen, J., Huang, W., 2011. Microstructure and residual stress of laser rapid formed Inconel 718 nickel-base superalloy. Opt. Laser Technol. 43, 208–213. https://doi.org/10.1016/j.optlastec.2010.06.015.

Ma, C., Han, E.-H., Peng, Q., Ke, W., 2018. Effect of polishing process on corrosion behavior of 308L stainless steel in high temperature water. Appl. Surf. Sci. 442, 423–436. https://doi.org/10.1016/j.apsusc.2017.12.190.

Mahalle, G., Salunke, O., Kotkunde, N., Gupta, A.K., Singh, S.K., 2019. Neural network modeling for anisotropic mechanical properties and work hardening behavior of Inconel 718 alloy at elevated temperatures. J. Mater. Res. Technol. 8, 2130–2140. https://doi.org/10.1016/j.jmrt.2019.01.019.

Mohammadian, N., Turenne, S., Brailovski, V., 2018. Surface finish control of additively-manufactured Inconel 625 components using combined chemical-abrasive flow polishing. J. Mater. Process. Technol. 252, 728–738. https://doi.org/10.1016/j.jmatprotec.2017.10.020.

Pal, P., Swarnalatha, V., Rao, A.V.N., Pandey, A.K., Tanaka, H., Sato, K., 2021. High speed silicon wet anisotropic etching for applications in bulk micromachining: a review. Micro Nano Syst. Lett. 9, 1–59. https://doi.org/10.1186/s40486-021-00129-0.

Rhodes, F.H., Barbour, C.B., 1923. The viscosities of mixtures of sulfuric acid and water. Ind. Eng. Chem. 15, 850–852.

Sánchez-Tovar, R., Leiva-García, R., García-Antón, J., 2015. Characterization of thermal oxide films formed on a duplex stainless steel by means of confocal-Raman microscopy and electrochemical techniques. Thin Solid Films 576, 1–10. https://doi.org/10.1016/j.tsf.2014.12.024.

Shamsaei, N., Yadollahi, A., Bian, L., Thompson, S.M., 2015. An overview of direct laser deposition for additive manufacturing; Part II: mechanical behavior, process parameter optimization and control. Addit. Manuf. 8, 12–35. https://doi.org/10.1016/j.addma.2015.07.002.

Shaw, D.W., 1981. Localized GaAs etching with acidic hydrogen peroxide solution. J. Electrochem. Soc. 128, 874–880.

Shi, Y., Pan, Q., Li, M., Huang, X., Li, B., 2014. Effect of Sc and Zr additions on corrosion behaviour of Al–Zn–Mg–Cu alloys. J. Alloys. Compd. 612, 42–50. https://doi.org/10.1016/j.jallcom.2014.05.128.

Shrestha, S., Starr, K., Chou, K., 2019. A study of keyhole porosity in selective laser melting: single-track scanning with micro-CT analysis. ASME J. Manuf. Sci. Eng 141, 1–23. https://doi.org/10.1115/1.4043622.

Sikora, E., Macdonald, D.D., 2002. Nature of the passive film on nickel. Electrochim. Acta 48, 69–77.

Skotheim, T.A., Reynolds, J., Elsenbamer, R., 1998. Handbook of Conducting Polymers Marcel Dekker, New York.

Sutow, E.J., 1980. The influence of electropolishing on the corrosion resistance of 316L stainless steel. J. Biomed. Mater. Res. 14, 587–595.

Thijs, L., Verhaeghe, F., Craeghs, T., Humbeeck, J.V., Kruth, J.-P., 2010. A study of the microstructural evolution during selective laser melting of Ti–6Al–4V. Acta Mater. 58, 3303–3312. https://doi.org/10.1016/j.actamat.2010.02.004.

Tian, Y., Gora, W.S., Cabo, A.P., Parimi, L.L., Hand, D.P., Tammas-Williams, S., Prangnell, P.B., 2018. Material interactions in laser polishing powder bed additive manufactured Ti6Al4V components. Addit. Manuf. 20, 11–22. https://doi.org/10.1016/j.addma.2017.12.010.

Ulutan, D., Ozel, T., 2011. Machining induced surface integrity in titanium and nickel alloys: a review. Int. J. Mach. Tools. Manuf. 51, 250–280. https://doi.org/10.1016/j.ijmachtools.2010.11.003.

Urlea, V., Brailovski, V., 2017. Electropolishing and electropolishing-related allowances for IN625 alloy components fabricated by laser powder-bed fusion. Int. J. Adv. Manuf. Technol 92, 4487–4499. https://doi.org/10.1007/s00170-017-0546-0.

Xia, Y., Kim, E., Mrksich, M., Whitesides, G.M., 1996. Chem. Mater. 8, 601–603.

Xin, H., Shi, Y., Ning, L., Zhao, T., 2016. Residual stress and affected layer in disc milling of titanium alloy. Mater. Manuf. Process. 31, 1645–1653. https://doi.org/10.1080/10426914.2015.1090583.

Yi, R., Zhang, Y., Zhang, X., Fang, F., Deng, H., 2020. A generic approach of polishing metals via isotropic electrochemical etching. Int. J. Adv. Manuf. Technol. 50, 103517 https://doi.org/10.1016/j.ijmachtools.2020.103517.

Zhang, Y., Lin, X., Yu, J., Guo, P., Li, J., Qin, T., Liu, J., Huang, W., 2020. Electrochemical dissolution behavior of heat treated laser solid formed Inconel718. Corros. Sci. 173, 108750 https://doi.org/10.1016/j.corsci.2020.108750.

Zhao, X., Chen, J., Lin, X., Huang, W., 2008. Study on microstructure and mechanical properties of laser rapid forming Inconel 718. Mater. Sci. Eng. A 478, 119–124. https://doi.org/10.1016/j.msea.2007.05.079.

Zhao, C., Qu, N., Tang, X., 2021. Electrochemical mechanical polishing of internal holes created by selective laser melting. J. Manuf. Process. 64, 1544–1562. https://doi.org/10.1016/j.jmapro.2021.03.003.